Article

Modeling the Topside Ionosphere Effective Scale Height through In Situ Electron Density Observations by Low-Earth-Orbit Satellites

Alessio Pignalberi [1,*], Michael Pezzopane [1], Tommaso Alberti [1], Igino Coco [1], Giuseppe Consolini [2], Giulia D'Angelo [2], Paola De Michelis [1], Fabio Giannattasio [1], Bruno Nava [3], Mirko Piersanti [4] and Roberta Tozzi [1]

1. Istituto Nazionale di Geofisica e Vulcanologia, Via di Vigna Murata 605, 00143 Roma, Italy
2. INAF-Istituto di Astrofisica e Planetologia Spaziali, Via del Fosso del Cavaliere 100, 00133 Roma, Italy
3. The Abdus Salam International Centre for Theoretical Physics, Strada Costiera 11, 34151 Trieste, Italy
4. Department of Physical and Chemical Sciences, University of L'Aquila, Via Vetoio, 67100 L'Aquila, Italy
* Correspondence: alessio.pignalberi@ingv.it

Abstract: In this work, we aim to characterize the effective scale height at the ionosphere F2-layer peak (H_0) by using in situ electron density (N_e) observations by Langmuir Probes (LPs) onboard the China Seismo-Electromagnetic Satellite (CSES—01). CSES—01 is a sun-synchronous satellite orbiting at an altitude of ~500 km, with descending and ascending nodes at ~14:00 local time (LT) and ~02:00 LT, respectively. Calibrated CSES—01 LPs N_e observations for the years 2019–2021 provide information in the topside ionosphere, whereas the International Reference Ionosphere model (IRI) provides N_e values at the F2-layer peak altitude for the same time and geographical coordinates as CSES—01. CSES—01 and IRI N_e datasets are used as anchor points to infer H_0 by assuming a linear scale height in the topside representation given by the NeQuick model. COSMIC/FORMOSAT—3 (COSMIC—1) radio occultation (RO) data are used to constrain the vertical gradient of the effective scale height in the topside ionosphere in the linear approximation. With the CSES—01 dataset, we studied the global behavior of H_0 for daytime (~14:00 LT) and nighttime (~02:00 LT) conditions, different seasons, and low solar activity. Results from CSES—01 observations are compared with those obtained through Swarm B satellite N_e-calibrated measurements and validated against those from COSMIC—1 RO for similar diurnal, seasonal, and solar activity conditions. H_0 values modeled by using CSES—01 and Swarm B-calibrated observations during daytime both agree with corresponding values obtained directly from COSMIC—1 RO profiles. Differently, H_0 modeling for nighttime conditions deserves further investigation because values obtained from both CSES—01 and Swarm B-calibrated observations show remarkable and spatially localized differences compared to those obtained through COSMIC—1. Most of the H_0 mismodeling for nighttime conditions can probably to be attributed to a sub-optimal spatial representation of the F2-layer peak density made by the underlying IRI model. For comparison, H_0 values obtained with non-calibrated CSES—01 and Swarm B N_e observations are also calculated and discussed. The methodology developed in this study for the topside effective scale height modeling turns out to be applicable not only to CSES—01 satellite data but to any in situ N_e observation by low-Earth-orbit satellites orbiting in the topside ionosphere.

Keywords: topside ionosphere modeling; effective scale height; China Seismo-Electromagnetic Satellite (CSES—01); Swarm B satellite; Langmuir probes data; International Reference Ionosphere (IRI) model; NeQuick model

1. Introduction

The topside ionosphere consists of the region extending from the F2-layer electron density peak to the overlying plasmasphere [1–3]. In this region, the electron density (N_e) decreases monotonically at a vertical rate driven by the vertical scale height (VSH, [4–6]),

which in turn depends on both the chemical composition of the plasma and its physical state. Since obtaining an accurate and thorough knowledge of plasma properties is difficult, an effective scale height is usually inferred from N_e measurements and used for empirical modeling. In the topside ionosphere, the effective scale height (H) is empirically obtained by fitting measured N_e values with different analytical functions, in order to obtain the most reliable representation of the topside vertical N_e distribution (e.g., [7–9]). As a consequence, calculated H values depend on the topside parameterization used for their calculation and can differ from VSH values derived from the plasma ambipolar diffusion theory [6].

Many empirical ionospheric models rely on the modeling of H for an accurate description of the N_e vertical profile. For instance, this is the approach pursued by the International Reference Ionosphere model (IRI, [10]), the NeQuick model [11], and the Empirical-Canadian High Arctic Ionospheric Model (E-CHAIM, [12]). Concerning the topside ionosphere, the modeling of H is challenging due to the reduced availability of data compared to the bottomside ionosphere, i.e., the region below the F2-layer peak. Indeed, the topside ionosphere is hidden to the widely spread ground-based ionosondes network, and N_e observations can be obtained only through more expensive techniques such as topside sounders satellites, in situ measurements by low-Earth-orbit (LEO) satellites, radio occultation (RO) of global navigation satellite system (GNSS) signals, and incoherent scatter radars (ISRs) [13]. The challenge in modeling the topside ionosphere comes in the form of IRI difficulties in properly representing the topside variations under both quiet and disturbed conditions (e.g., [14]). As a result, the availability of new topside N_e observations provides the opportunity to improve the description of H and, consequently, the topside N_e modeling. This is the main motivation driving the present investigation.

In this work, we characterize the global behavior of the topside effective scale height by using in situ N_e observations by Langmuir Probes (LPs) onboard the China Seismo-Electromagnetic Satellite (CSES—01) and Swarm B LEO satellites. CSES—01 is dedicated to geophysical measurements and near-Earth environment monitoring, with a focus on the investigation of the electromagnetic perturbations possibly associated with earthquakes [15]. Swarm B is one of the three satellites of the Swarm constellation launched by the European Space Agency at the end of 2013 with the main aim of studying the geomagnetic field, the electric currents in the magnetosphere and ionosphere, and the impact of solar wind on the dynamics of the upper atmosphere [16].

In situ N_e observations from LEO satellites alone cannot provide information on H and then on the N_e vertical variation. They must be accompanied with N_e observations collected at different altitudes, by different instruments, or by modeled values. For example, the authors of [7], using in situ N_e observations made by Swarm satellites as the topside anchor point and the IRI UP data-assimilation modeled values over Europe [17] as the F2-layer peak anchor point, inferred a constant H by using different topside functions. A similar approach was also later pursued by the authors of [18] to calculate the value of the effective scale height at the F2-layer peak (H_0) to be used in the NeQuick topside model scale height formulation [11,19]. The above-mentioned works were confined to the European region due to the use of the IRI UP model for the F2-layer peak anchor point and were based on the assumption of constant H in the topside [7] and on the topside H representation used by the NeQuick model [18]. In the present work, we relaxed these constraints in the calculation of the topside effective scale height. The use of IRI to model the F2-layer peak anchor point allows for the global modeling of H with CSES—01 and Swarm B in situ N_e observations. Later in this paper, we include a linear variation in the topside H description based on evidence from several works [6,20–26]. To include the linear variation in the H description, we take advantage of COSMIC/FORMOSAT—3 (also known as COSMIC—1 [27]) RO measurements. COSMIC—1 RO N_e topside profiles are used to infer the median behavior of the effective scale height vertical gradient in the topside through the methodology developed by [6,25]. The linear H description can be then applied to N_e datasets provided by in situ LEO satellites, along with IRI-modeled F2-layer peak parameters, to derive values of H_0.

The remainder of this paper is organized as follows: Section 2 includes a description of CSES—01 and Swarm B in situ N_e datasets and the calibration applied to them; the same section describes COSMIC—1 RO N_e data and IRI-modeled data. On one hand, Section 3 describes in detail the topside effective scale height modeling methodology based on the H linear approximation in the NeQuick topside model and, on the other hand, how H_0 values are obtained. Section 4 presents the global behavior of H_0 for daytime and nighttime conditions, different seasons, and for the low solar activity years covered by our dataset. Results from CSES—01 observations are compared with those derived from Swarm B observations and validated against those derived from COSMIC—1 RO. Also for comparison, H_0 values obtained with non-calibrated CSES—01 and Swarm B N_e observations are calculated and discussed. In Section 4, results obtained through the use of the original NeQuick topside formulation are also presented. Moreover, a comparison between COSMIC—1-measured and IRI-modeled F2-layer peak parameters is provided. Section 5 discusses the results of Section 4, while Section 6 outlines the conclusions that can be drawn from the present study.

2. Data Description

2.1. CSES—01 Langmuir Probe Observations

CSES—01 is a sun-synchronous LEO satellite launched on the 2nd of February 2018 at an initial altitude of 507 km [15]. The orbit has an inclination of 97.4°, with descending and ascending nodes at ~14:00 Local Time (LT) and ~02:00 LT, respectively. CSES—01 observations cover the latitudinal range between 70° S and 70° N. CSES—01 LP data are freely available at https://www.leos.ac.cn/ (accessed on 7 April 2023) after registration. LPs onboard CSES—01 provide in situ N_e observations in a range between $5 \cdot 10^2$ cm^{-3} and $1 \cdot 10^7$ cm^{-3} [28,29]. The sampling rate of LP observations depends on the geographical location according to two operational modes: survey and burst. In burst mode, LP observations' sampling rate is 1.5 s and activates only over China and within the main seismic zones [15]. In survey mode, the sampling rate is 3 s.

In this work, we consider CSES—01 LP N_e observations from the 1st of January 2019 to the 30th of September 2021. The dataset consists of 13,957 semi-orbits in the daytime sector (~14:00 LT) and 13,978 in the nighttime sector (~02:00 LT). Both survey and burst mode data are used.

Several studies compared and validated CSES—01 LP N_e observations against observations made by incoherent scatter radars and similar LEO satellites, as well as against corresponding values provided by ionospheric models [30–34]. There is good agreement among these studies in highlighting a general underestimation of N_e values recorded by CSES—01 when compared to different data sources. Nevertheless, CSES—01 LP N_e observations succeed in describing both the spatial and diurnal N_e patterns in the topside ionosphere. Since the reliability of both the magnitude and variations of N_e values is needed for the calculation of the topside effective scale height, we applied the CSES—01 LP N_e calibration procedure developed by the authors of [34]. This calibration is based on the comparison with Swarm B satellite LP and Face Plate (FP) N_e observations and was validated against ISRs observations.

Following [34], original CSES—01 N_e measured values (in cm^{-3}) have been calibrated by applying the following equations:

$$
\begin{cases}
y = 10^{\frac{x-q}{m}}, \\
x \equiv \log_{10}(\text{CSES-01 LP original } N_e), \\
y \equiv \log_{10}(\text{CSES-01 LP calibrated } N_e).
\end{cases}
\tag{1}
$$

where the m and q calibration coefficients were calculated for the daytime and nighttime sectors:

$$\text{daytime} \Rightarrow \begin{cases} m = 0.888 \pm 0.013; \\ q = -0.203 \pm 0.063; \end{cases}$$
$$\text{nighttime} \Rightarrow \begin{cases} m = 0.938 \pm 0.009; \\ q = -0.073 \pm 0.038. \end{cases} \tag{2}$$

This calibration procedure holds for the low solar activity conditions covered by the datasets used for its development. The shortness of the dataset and the FP data limitations did not allow for the investigation of the possible seasonal variations of calibration parameters [34].

Since the CSES—01 dataset used in this paper is the same as that used in [34], the application of this calibration procedure to our dataset is straightforward. For comparison purposes, in the following, both original and calibrated CSES—01 LP N_e observations will be used. The authors of [34] demonstrated how this calibration procedure strongly reduces the CSES—01 N_e underestimation for both daytime and nighttime conditions, with calibrated values in agreement with corresponding values measured by Arecibo, Jicamarca, and Millstone Hill ISRs.

2.2. Swarm B Langmuir Probe Observations

Swarm is a constellation of three LEO satellites launched on the 22nd of November 2013 and is still in operation [16]. Among the three satellites, Swarm B has a circular near-polar orbit with an inclination of 87.75° and an initial altitude of around 500–510 km, which is similar to that of CSES—01. In contrast to CSES—01, Swarm B spans all the LTs in about 130–140 days. Swarm B provides in situ N_e observations through two different instruments of the Electric Field Instrument (EFI) payload [35]: spherical LPs and the FP of the Thermal Ion Imager (TII). LPs provide continuous N_e observations at 2-Hz rate, while the FP has a 16-Hz rate; however, corresponding observations are not continuous in time [35–38]. Swarm data are freely downloadable at https://earth.esa.int/eogateway/missions/swarm/data (accessed on 7 April 2023).

In this work, we consider Swarm B LP N_e observations in the same time window as the CSES—01 dataset, i.e., from the 1st of January 2019 to the 30th of September 2021. To be consistent with the CSES—01 dataset, we also considered only Swarm B observations in the range between 70° S and 70° N in terms of geographic latitude, and for the two LT sectors sounded by CSES—01. Specifically, we selected Swarm B observations in the range 01:00 ≤ LT < 03:00 for the nighttime sector and in the range 13:00 ≤ LT < 15:00 for the daytime sector [34].

In a similar manner to CSES—01, Swarm B LP N_e observations also underwent a calibration procedure based on the results of [34]. In fact, the authors of [34,39,40] independently highlighted how Swarm B LP N_e observations are characterized by a nighttime overestimation under low solar activity conditions. To overcome this issue, the authors of [34] calibrated Swarm B LP N_e observations on the basis of corresponding values from the FP onboard the same satellite, which showed a much better agreement with ISRs observations. Additionally, original Swarm B LP N_e measured values (in cm^{-3}) have been calibrated by applying Equation (1), where $x \equiv \log_{10}(\text{Swarm B LP original } N_e)$ and $y \equiv \log_{10}(\text{Swarm B LP calibrated } N_e)$, with calibration coefficients:

$$\text{daytime} \Rightarrow \begin{cases} m = 0.978 \pm 0.009; \\ q = 0.161 \pm 0.044; \end{cases}$$
$$\text{nighttime} \Rightarrow \begin{cases} m = 1.374 \pm 0.017; \\ q = -1.254 \pm 0.069. \end{cases} \tag{3}$$

The application of the calibration procedure to Swarm B LP N_e values allows one to fix the nighttime overestimation for low solar activity conditions [34]. For daytime conditions,

its application has only marginal effects, meaning that the agreement between LP and FP data is already good.

2.3. IRI F2-Layer Peak Modeled Characteristics

IRI is an empirical climatological model of the ionosphere, which is considered the reference model by the ionospheric community [10,41]. The last version of the model, i.e., IRI—2020, has been considered in this study to obtain information on the F2-layer peak characteristics $NmF2$ and $hmF2$, which are the electron density and altitude of the F2-layer peak. IRI was run for the same time periods and locations covered by both CSES—01 and Swarm B datasets. $NmF2$ values were modeled through the URSI coefficients [42]. $hmF2$ values are those given by the Shubin option [43]. Both are recommended options in IRI—2020. Information about the performance of IRI in describing the F2-layer peak characteristics for different conditions and on a global basis can be found in [44]. IRI—2020 Fortran code is available on the IRI website (http://irimodel.org/, accessed on 7 April 2023).

2.4. COSMIC/FORMOSAT—3 Radio Occultation Observations

COSMIC/FORMOSAT—3 (COSMIC—1 in brief) was a six LEO-microsatellites constellation launched on the 15th of April 2006 and decommissioned in 2020 [27]. COSMIC—1 satellites had circular orbits with an inclination of $72°$, an altitude of about 800 km, and a longitudinal separation between neighboring satellites of about $30°$. Each satellite was equipped with a Global Positioning System (GPS) RO receiver capable of measuring the phase delay of radio waves from GPS satellites as they are occulted by the Earth's atmosphere. Through data inversion, RO measurements provide ionospheric N_e values at the tangent points of the radio occultation—from the ground to the COSMIC—1 satellites altitude. COSMIC—1 RO data are based on the Abel inversion technique [45,46], which assumes a spherical symmetry in the ionosphere. It is worth noting that this working hypothesis can be violated in locations where strong horizontal electron density gradients are present. The equatorial ionization anomaly region, geomagnetically disturbed conditions, and the hours around the solar terminator are the most affected by such an issue [47,48].

COSMIC—1 RO *ionprf* files containing N_e quasi-vertical profiles are stored in the COSMIC Data Analysis and Archive Center (CDAAC, http://cdaac-www.cosmic.ucar.edu/cdaac/products.html, accessed on 7 April 2023) [49].

In this work, to be consistent with the CSES—01 dataset, we considered COSMIC—1 RO observations in the range $00:00 \leq LT < 04:00$ for the nighttime sector and in the range $12:00 \leq LT < 16:00$ for the daytime sector. The LT sectors in which we selected COSMIC—1 RO observations are wider than those used in the Swarm B LT selection (Section 2.2) to ensure the consideration of a statistically significant number of RO profiles. Moreover, only COSMIC—1 RO data measured when the 81-day running mean ($F10.7_{81}$) of the solar flux index F10.7 [50] was lower or equal than 85 sfu (solar flux unit) has been considered, i.e., for the same low solar activity conditions of the CSES—01 dataset.

3. Topside Effective Scale Height Calculation Methodology

The topside effective scale height calculation methodology here proposed is based on the NeQuick model topside N_e representation [11], with an empirical linear topside effective scale height. The parameters of the linear topside scale height are obtained through N_e observations from in situ LEO satellites, COSMIC—1 RO profiles, and IRI-modeled F2-layer peak characteristics.

3.1. NeQuick Model Topside Representation and Effective Scale Height Linear Approximation

The NeQuick model describes the topside ionosphere through a semi-Epstein layer anchored at the F2-layer peak [11,19,25]:

$$N_e(h) = 4NmF2 \frac{\exp\left(\frac{h - hmF2}{H}\right)}{\left[1 + \exp\left(\frac{h - hmF2}{H}\right)\right]^2}. \tag{4}$$

The N_e decrease with height is driven by the empirical effective scale height H, which the NeQuick model describes with the following formulation:

$$H(h) = H_0 \left[1 + \frac{rg(h - hmF2)}{rH_0 + g(h - hmF2)}\right]. \tag{5}$$

According to (5), H is a function of the three empirical topside parameters: H_0, g, and r. H_0 is the scale height value at the F2-layer peak; g represents the scale height vertical gradient near the F2-layer peak; r is the parameter controlling the H behavior very distant from the F2-layer peak. The NeQuick model calculates H_0 from F2-layer and bottomside parameters [11], while $g = 0.125$ and $r = 100$.

The formulation (5) was designed to allow a smooth transition from the linear behavior near the F2-layer peak to the non-linear behavior in the overlying plasmasphere. The authors of [6,23,25] investigated the altitudinal range in which the H linear approximation holds. Using topside sounder data, the authors of [23] found that the H linear approximation is valid up to 1300 km above the F2-layer peak. The authors of [6,25] found similar results using COSMIC—1 RO data up to the maximum altitude sounded by COSMIC—1 satellites, i.e., 800 km from ground. As a consequence, as demonstrated by the authors of [23] and [6,25], the H linear approximation is well-verified at the altitudes of CSES—01 and Swarm B orbits (~500 km from ground), and there is no added value in introducing the non-linear terms in the H modeling. Then, we did not apply the NeQuick non-linear formulation of Equation (5) and relied on the linear approximation given by:

$$\begin{cases} H(z) = \frac{dH}{dz}z + H_0, \\ z \equiv h - hmF2, \end{cases} \tag{6}$$

where the slope dH/dz represents the vertical gradient of the modeled topside linear scale height, while the intercept H_0 represents the value at the F2-layer peak ($h = hmF2$ at $z = 0$).

An exact application of Equation (6) requires the knowledge of the H topside vertical profile. The authors of [25] developed a mathematical procedure to obtain H values from F2-layer peak and topside N_e values through the NeQuick topside formulation of Equation (4):

$$H_{\text{Epstein}}(h) = \frac{h - hmF2}{\ln\left\{\frac{1}{N_e(h)}\left[(2NmF2 - N_e(h)) + 2\sqrt{NmF2^2 - N_e(h) \cdot NmF2}\right]\right\}}. \tag{7}$$

H_{Epstein} is the effective scale height obtained by mathematically inverting the semi-Epstein topside formulation of Equation (4).

According to (7), when the F2-layer peak characteristics ($NmF2$ and $hmF2$) and the $N_e(h)$ topside profile are both available from observations, an $H_{\text{Epstein}}(h)$ profile can be obtained for the entire topside profile. This is the case with COSMIC—1 RO profiles, which allow for the calculation of $H_{\text{Epstein}}(h)$ through Equation (7), as well as allow for the obtainment of dH/dz and H_0 values by fitting Equation (6) to the calculated $H_{\text{Epstein}}(h)$ values [25]. The same approach used by the authors of [25] cannot be applied to CSES—01 and Swarm B satellite data because only the in situ N_e value is provided by satellites. To

apply Equation (6) to in situ LEO satellite observations, we need to constrain dH/dz in Equation (6) by using additional information provided by COSMIC—1 RO observations.

3.2. Topside Effective Scale Height Vertical Gradient Modeling

To gain information on the dH/dz median behavior, we applied the procedure developed in [25], as briefly outlined in Section 3.1, to the COSMIC—1 RO dataset described in Section 2.4. Figure 1 depicts an example of topside H calculation and modeling with data measured by COSMIC—1 on the 11th of October 2011 at 10:19:45 UT (Universal Time) at latitude = 39.86° N and longitude = 0.69° E. Topside $N_e(h)$ values measured by COSMIC—1—represented by blue points in panel (a)—are used to calculate $H_{Epstein}(h)$ through Equation (7)—represented as blue points in panel (b). Calculated $H_{Epstein}(h)$ values show a clear linear dependence with height. The fit of Equation (6) to the calculated $H_{Epstein}(h)$ values allows for the obtainment of the linear fit parameters, i.e., dH/dz (the slope) and H_0 (the intercept). $H(z)$ values obtained with fitting parameters are represented as the red line in panel (b). By using calculated $H(z)$ values as the effective scale height in the NeQuick topside representation of Equation (4), we obtain the $N_e(h)$ topside profile—represented by the red curve in panel (a). The comparison between $N_e(h)$ values measured by COSMIC—1 and those modeled by using $H(z)$ assumes that it is possible to accurately reproduce the topside profile with the linear approximation of the effective scale height. This assumption is true in the range of altitudes covered by COSMIC—1 observations [25].

For each COSMIC—1 RO profile, we obtain a couple of linear parameters (dH/dz, H_0). We applied this procedure to the selected COSMIC—1 RO dataset, which covers the diurnal and solar activity conditions probed by CSES—01. H_0 values from COSMIC—1 have been used as references for comparison (see Section 4), while dH/dz values are used in the topside H modeling along with CSES—01 and Swarm B observations.

Since the topside ionosphere exhibits seasonal variations, we binned calculated dH/dz values as a function of the months of the year in four bins around solstices and equinoxes:

- NDJ: November, December, January—the months around the December solstice;
- FMA: February, March, April—the months around the March equinox;
- MJJ: May, June, July—the months around the June solstice;
- ASO: August, September, October—the months around the September equinox.

Ref. [51] highlighted also how topside parameters are strongly connected with the geomagnetic field lines configuration. Then, magnetic coordinates are the natural basis for a spatial description of the topside parameters. Therefore, we further binned dH/dz values as a function of the Quasi-Dipole (QD) geomagnetic latitude [52], from 90° S to 90° N in steps of 2.5°. Figure 2 represents the dH/dz mean values as a function of QD latitude for the four seasons and for the two LT sectors encompassed by CSES—01 orbit. Error bars are the standard deviation values inside each bin. dH/dz ranges between 0.1 and 0.3, with very large differences between daytime and nighttime conditions and large seasonal variations during nighttime. During daytime, dH/dz shows an absolute minimum at the geomagnetic equator and values increasing with latitude. This pattern is consistent across different seasons. Conversely, in the nighttime sector, dH/dz shows large seasonal variations with maxima at mid latitudes. At equinoxes (red and blue curves), dH/dz maximizes at mid latitudes in both hemispheres, with small hemispheric differences. Instead, at solstices, dH/dz maximizes in the winter hemisphere at mid latitudes. Such seasonal differences support the need to include seasonal dependence in the modeling. The mean dH/dz values seen in Figure 2 are used to apply the linear scale height formulation to CSES—01 and Swarm B observations.
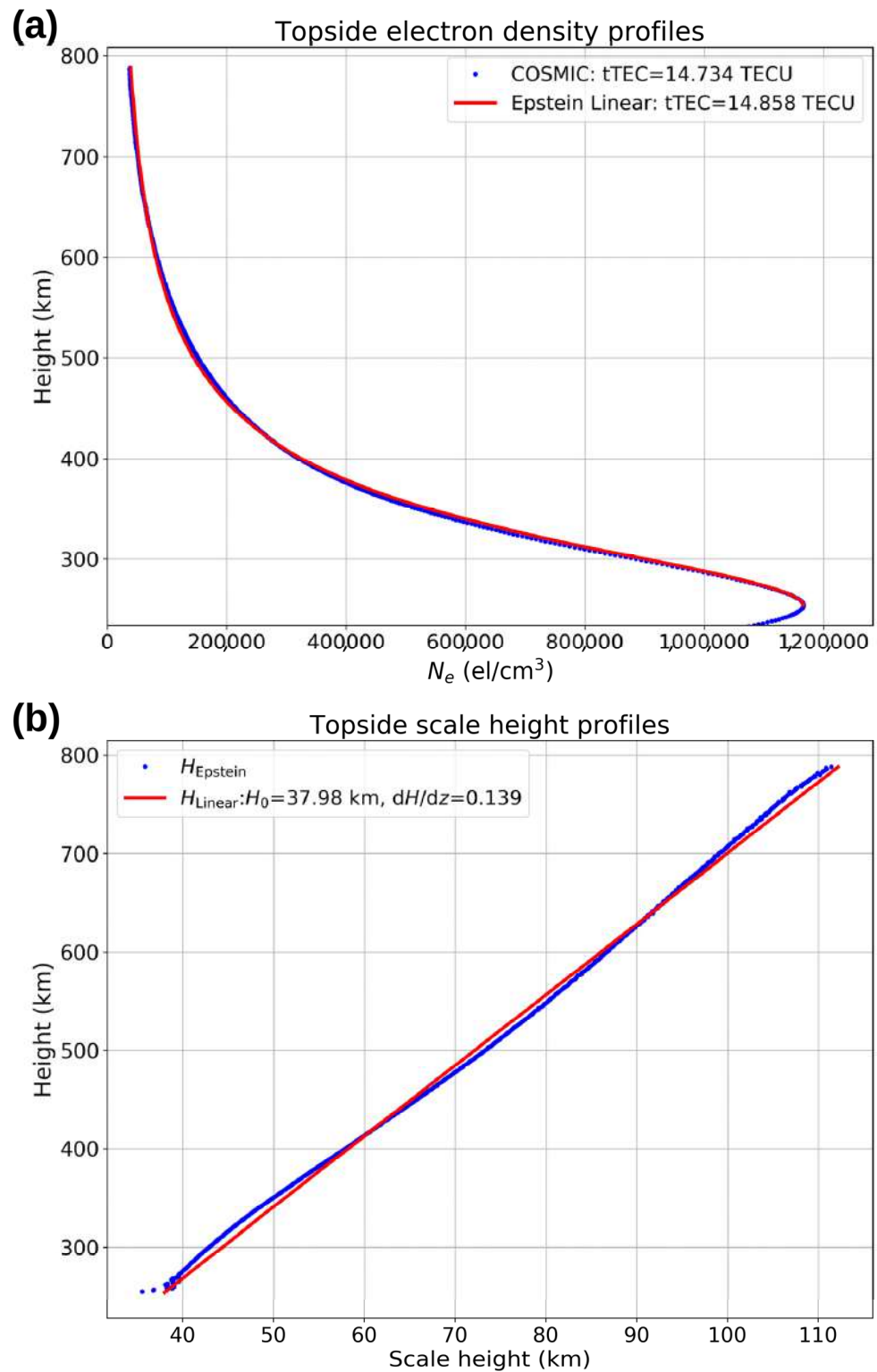
(a)

(b)

Figure 1. Panel (**a**), topside N_e values measured by COSMIC—1 (blue points) and modeled by using the topside linear scale height (H_{Linear}) (red line). Panel (**b**), topside scale height values $H_{Epstein}$ (blue points) obtained from the COSMIC—1 measured N_e profile and corresponding modeling through a linear fit (red line). Data from COSMIC—1 ionPrf_C001.2011.284.10.20.G23_2013.3520_nc file, measured on the 11th of October 2011 at 10:19:45 UT at latitude = 39.86° N and longitude = 0.69° E are used.
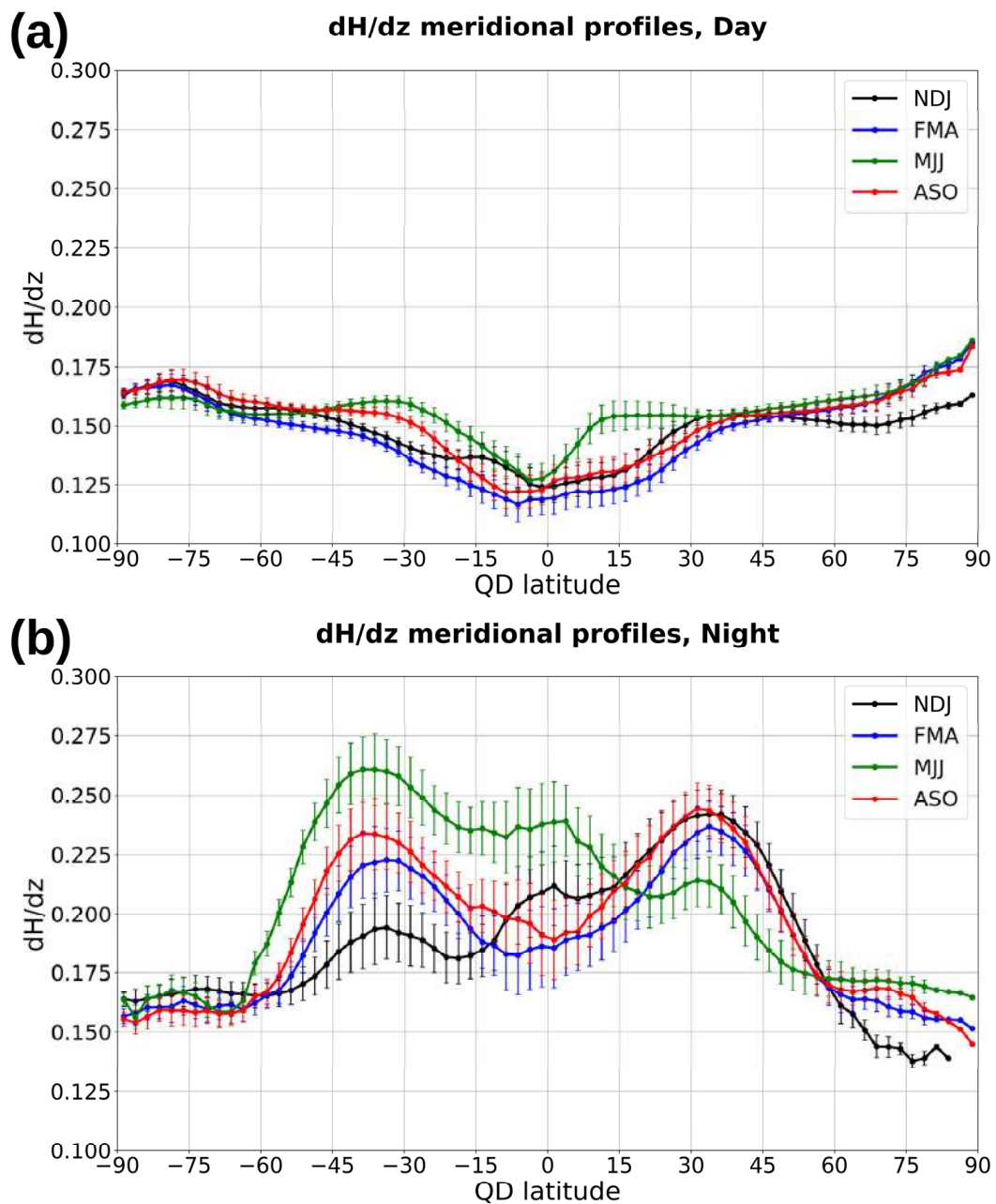
(a)

(b)

Figure 2. Vertical gradient dH/dz of the topside scale height, as obtained by COSMIC—1 and as a function of QD magnetic latitude, for low solar activity. Panel (**a**) is for the daytime sector (~14:00 LT), while panel (**b**) is for the nighttime sector (~02:00 LT). Colored curves are for different months: NDJ = (November, December, January) in black; FMA = (February, March, April) in blue; MJJ = (May, June, July) in green; and ASO = (August, September, October) in red. Points are mean values; error bars are standard deviation values.

3.3. Modeling the Effective Scale Height at the F2-Layer Peak through In Situ LEO N_e Observations

We model the topside effective scale height in the linear approximation assumption (6), with the vertical gradient provided by COSMIC—1 RO data, through the NeQuick topside formulation (4). The information given by CSES—01 and Swarm B in the topside and by IRI model at the F2-layer peak are used to calculate the effective scale height at the F2-layer peak, i.e., H_0. Figure 3 depicts an example applied to a CSES—01 measurement performed on the 24th of January 2020 at 12:55:10 UT—latitude = $-26.88°$, longitude = $10.77°$,

QD latitude = $-35.95°$—along a daytime orbit. Specifically, for that time, CSES—01 LP measures an electron density value of 95,496 cm^{-3} at the height of 507.0 km (green point in Figure 3); at the same time and geographical location, IRI models an F2-layer peak with NmF2 = 416,130 cm^{-3} at hmF2 = 254.3 km (red point in Figure 3). These two points represent the topside and F2-layer peak anchor points, respectively. For those daytime conditions, month, and QD latitude, from Figure 2, we obtain a value of dH/dz equal to 0.147. At this point, starting from the F2-layer peak anchor point and having fixed dH/dz = 0.147, we vary H_0 in Equation (6) and input H in the NeQuick topside formulation (4) until we obtain a match with the measured topside N_e anchor point. In Figure 3, H_0 = 55.4 km is the optimal value found for H_0, i.e., the value for joining the two anchor points with the NeQuick topside formulation with a linear scale height. The topside N_e profile is the blue curve in Figure 3. The procedure just described has been applied to every CSES—01 and Swarm B LPs measurement in the datasets described in Section 2. This allowed for the obtainment of a large dataset of modeled H_0 values from both CSES—01 and Swarm B datasets. Moreover, we used both calibrated and non-calibrated CSES—01 and Swarm B observations for comparison purposes.
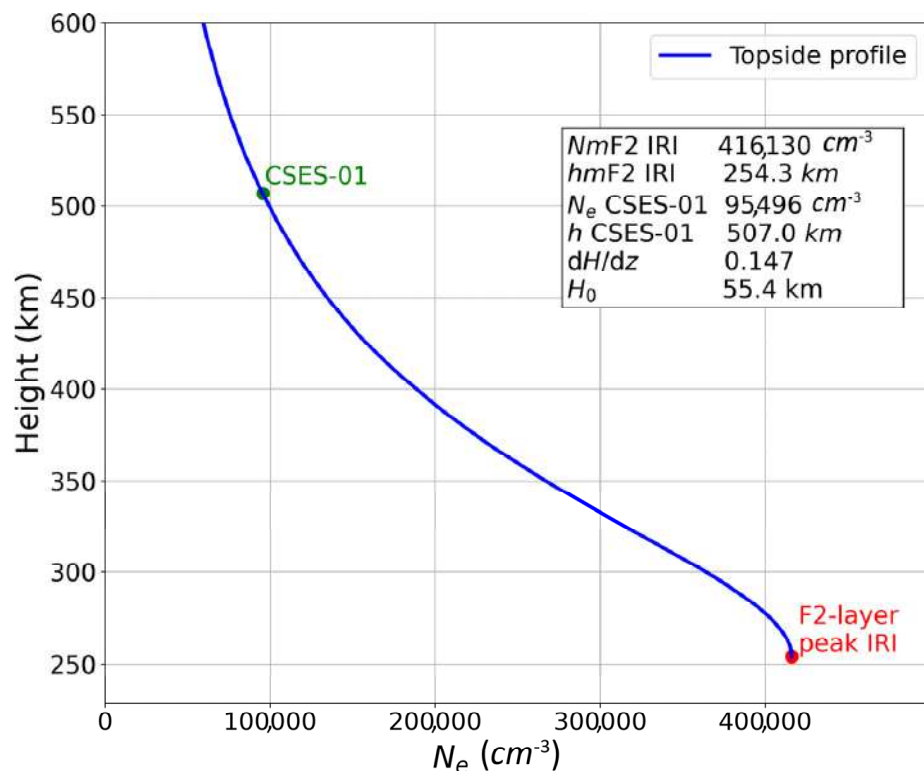

Figure 3. Example of methodology employed for the topside N_e profile modeling. The red point is the F2-layer peak anchor point, as modeled by IRI; the green point is the topside anchor point, as measured by CSES—01 (calibrated values); the blue curve is the topside N_e profile, which was obtained via the modeled linear scale height. Anchor points, values, and linear scale height fit parameters are reported in the textbox. CSES—01 data were recorded on the 24th of January 2020 at 12:55:10 UT—latitude = $-26.88°$, longitude = $10.77°$, QD latitude = $-35.95°$ for daytime conditions (~14:00 LT).

4. Results

4.1. Topside Effective Scale Height from Calibrated In Situ N_e Observations

To highlight the time and spatial behavior of H_0 values calculated through the procedure outlined in Section 3, we binned data in geographical coordinates for different diurnal and seasonal conditions. Since our dataset embraces only low solar activity conditions (F10.7$_{81}$ ≤ 85 sfu), no solar activity sorting has been applied. Data were sorted in two

bins in local time according to the CSES—01 orbital configuration. The process of seasonal sorting is the same as the one applied in Section 3.2. For each of these bins, data were sorted in bins 2°-wide in latitude and 4°-wide in longitude. The median value of H_0 inside each geographical bin was considered.

Figure 4 shows the geographical maps of median H_0 values for the daytime sector. First column plots are H_0 values obtained with CSES—01 calibrated N_e values; second column plots are obtained with Swarm B calibrated N_e values; while third column plots are H_0 values obtained directly from COSMIC—1 RO topside profiles. COSMIC—1 H_0 values are considered as the reference here because RO observations allow for the calculation of H_0 by directly applying Equation (6) to H_{Epstein} values calculated through Equation (7), without any assumption and use of modeled values.
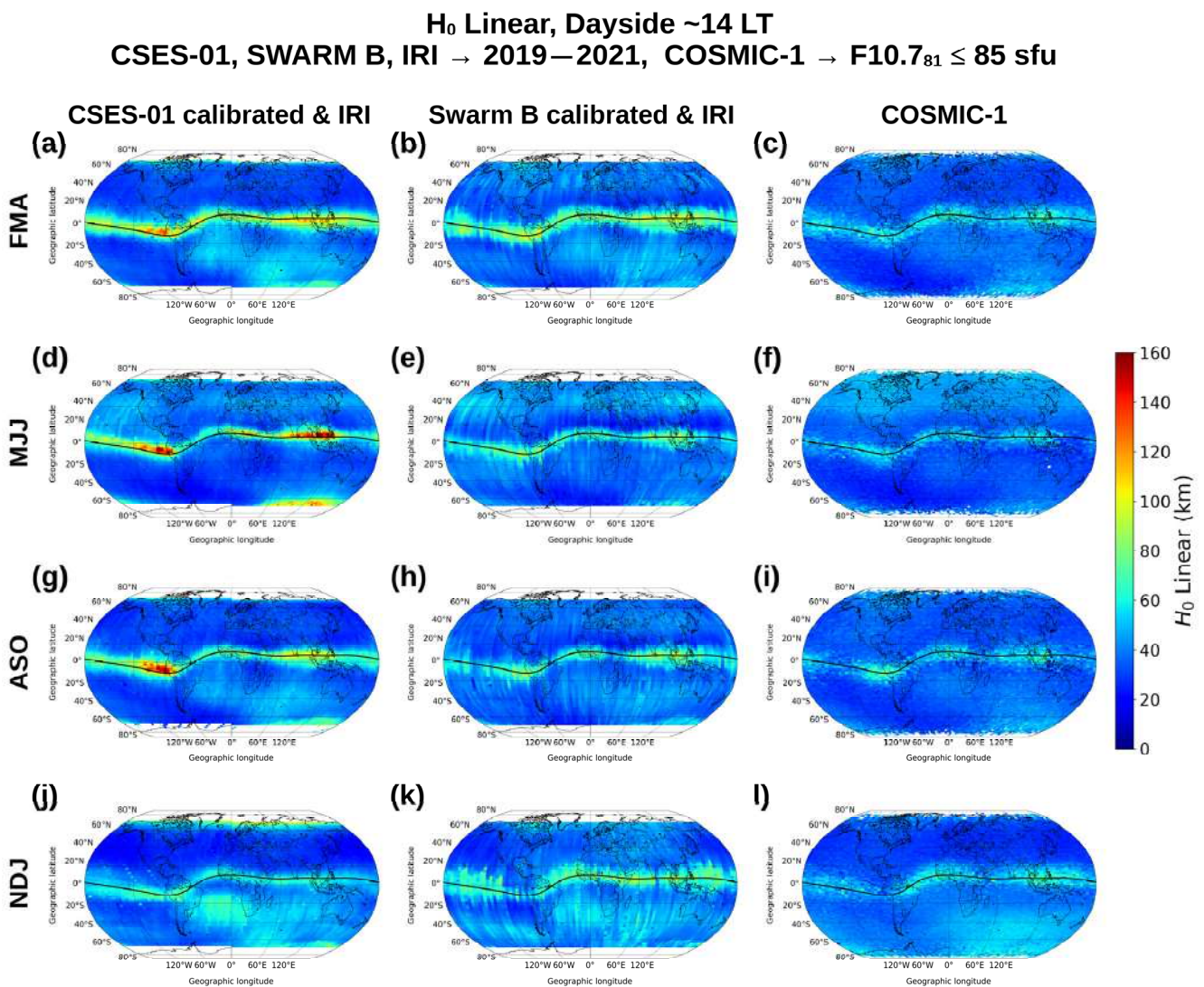

Figure 4. Geographical representation of median values of H_0 for the daytime sector (~14:00 LT). First row plots (panels (**a**–**c**)) are for FMA = (February, March, April) months; second row plots (panels (**d**–**f**)) for MJJ = (May, June, July) months; third row plots (panels (**g**–**i**)) for ASO = (August, September, October) months; and fourth row plots (panels (**j**–**l**)) for NDJ = (November, December, January) months. First column plots (panels (**a**,**d**,**g**,**j**)) are H_0 values obtained with calibrated CSES—01 and IRI-modeled data; second column plots (panels (**b**,**e**,**h**,**k**)) are corresponding values obtained with calibrated Swarm B and IRI-modeled data; third column plots (panels (**c**,**f**,**i**,**l**)) are those obtained with COSMIC—1-measured N_e data by radio occultation. Color bar scale is the same across all panels. The solid black curve in each plot represents the geomagnetic equator.

Daytime H_0 values show an absolute maximum in a narrow belt around the geomagnetic equator (highlighted by a solid black curve in the maps), while much lower values are found outside of this region. H_0 values are slightly higher at the highest latitudes. Although the three datasets show similar spatial patterns, they differ in magnitude near the geomagnetic equator, where values modeled using both CSES—01 and Swarm B observations show much higher values than those obtained through COSMIC—1. Specifically, H_0 values from CSES—01 reach values higher than 150 km in MJJ and ASO months in the range of longitudes between 60°E and 120°E and between 60°W and 120°W. Similar longitudinal variations are also seen by Swarm B and COSMIC—1, albeit with lower values in magnitude. The orbital configuration of CSES—01 turns out to be well-suited for studying longitudinal variations. For example, CSES—01 successfully captures the H_0 increase in the South Atlantic region, which is especially visible in the NDJ and FMA months. This region corresponds to the South Atlantic anomaly, where the magnitude of the geomagnetic field decreases noticeably. Seasonal differences are visible near the geomagnetic equator and at mid latitudes. Indeed, at mid latitudes, H_0 values are higher in the local summer season (MJJ in the Northern hemisphere; NDJ in the Southern hemisphere) than in the local winter. Around equinoxes, hemispheric differences are limited to the longitudinal sectors of the South Atlantic and South Indian oceans.

Figure 5 shows the geographical maps of median H_0 values for the nighttime sector in the same format as Figure 4. Compared to daytime, in the nighttime sector, H_0 values obtained from both CSES—01 and Swarm B observations show large differences compared to COSMIC—1, as well as a greater spatial variability. In particular, CSES—01 and Swarm B predict higher H_0 values in several latitudinal belts at both low and mid latitudes. The region of very high H_0 values in the South African and South Indian ocean is also noteworthy, with values significantly higher compared to other longitudinal sectors at the same latitude. The highest values are obtained during the NDJ months, regardless of the local season. On the other hand, COSMIC—1 shows a much simpler spatial pattern, with higher values at high latitudes (within the auroral oval region) and lower values at mid and low latitudes.

4.2. Topside Effective Scale Height from Non-Calibrated In Situ N_e Observations

In Section 4.1, we showed H_0 values obtained by using CSES—01 and Swarm B N_e values calibrated according to [34]. For comparison, in this section, we show corresponding results obtained with original (i.e., non-calibrated) CSES—01 and Swarm B N_e values.

Figure 6 shows geographical maps of median H_0 values obtained with non-calibrated CSES—01 and Swarm B N_e values for the daytime sector. COSMIC—1 values are the same as those used in Figure 4. By using non-calibrated N_e values, the CSES—01 H_0 values are much lower than those of Figure 4, ranging between 0 and 20 km. Such H_0 values are very low when compared to corresponding values found by other authors by using different methodologies and datasets [21–24,26,51,53]. H_0 values ranging between 0 and 20 km would cause a decrease in electron density in the topside ionosphere at a much faster rate than is usually observed. This is an independent piece of evidence that demonstrates the importance of calibrating CSES—01 N_e values in order to reliably reproduce the topside ionosphere profile shape. On the other hand, H_0 values from non-calibrated Swarm B N_e values are very similar to those obtained with calibrated values. This is not surprising, given that the calibration has only a minor effect on Swarm B during the daytime, as highlighted in Section 2.2 and by the authors of [34].

H$_0$ Linear, Nightside ~02 LT
CSES-01, SWARM B, IRI → 2019−2021, COSMIC-1 → F10.7$_{81}$ ≤ 85 sfu

CSES-01 calibrated & IRI **Swarm B calibrated & IRI** **COSMIC-1**
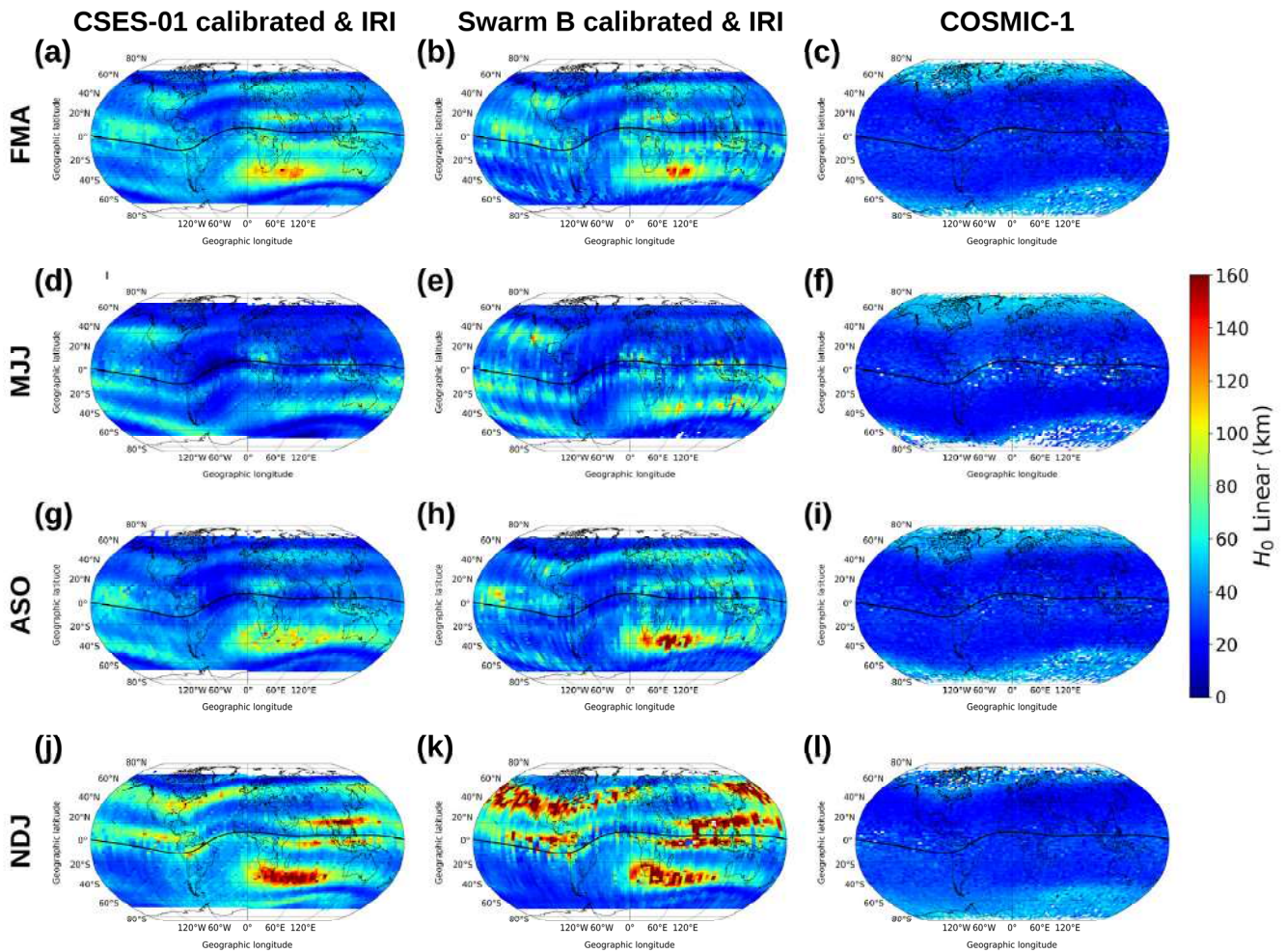

Figure 5. Geographical representation of median values of H_0 for the nighttime sector (~02:00 LT). First row plots (panels (**a**–**c**)) are for FMA = (February, March, April) months; second row plots (panels (**d**–**f**)) for MJJ = (May, June, July) months; third row plots (panels (**g**–**i**)) for ASO = (August, September, October) months; and fourth row plots (panels (**j**–**l**)) for NDJ = (November, December, January) months. First column plots (panels (**a**,**d**,**g**,**j**)) are H_0 values obtained with calibrated CSES—01 and IRI-modeled data; second column plots (panels (**b**,**e**,**h**,**k**)) are corresponding values obtained with calibrated Swarm B and IRI-modeled data; third column plots (panels (**c**,**f**,**i**,**l**)) are those obtained with COSMIC—1-measured N_e data by radio occultation. Color bar scale is the same across all panels. The solid black curve in each plot represents the geomagnetic equator.

Figure 7 shows geographical maps of median H_0 values obtained with non-calibrated CSES—01 and Swarm B N_e values for the nighttime sector. As expected, H_0 values from non-calibrated CSES—01 N_e values show values much lower than those of Figure 5, according to the original N_e underestimation by CSES—01. Instead, H_0 values from non-calibrated Swarm B N_e values show a remarkable general increase. This increase is so high that, in many bins, it was not possible to calculate H_0 because Swarm B N_e values were higher than $NmF2$ values modeled by IRI; this fact is well-highlighted by the blank bins in the NDJ months. This is due to the Swarm B N_e overestimation during nighttime and low solar activity conditions evidenced by the authors of [34,38,40]. Without any correction, original Swarm B N_e values recorded in these specific conditions would produce an excessive and non-physical topside effective scale height.

H$_0$ Linear, Dayside ~14 LT
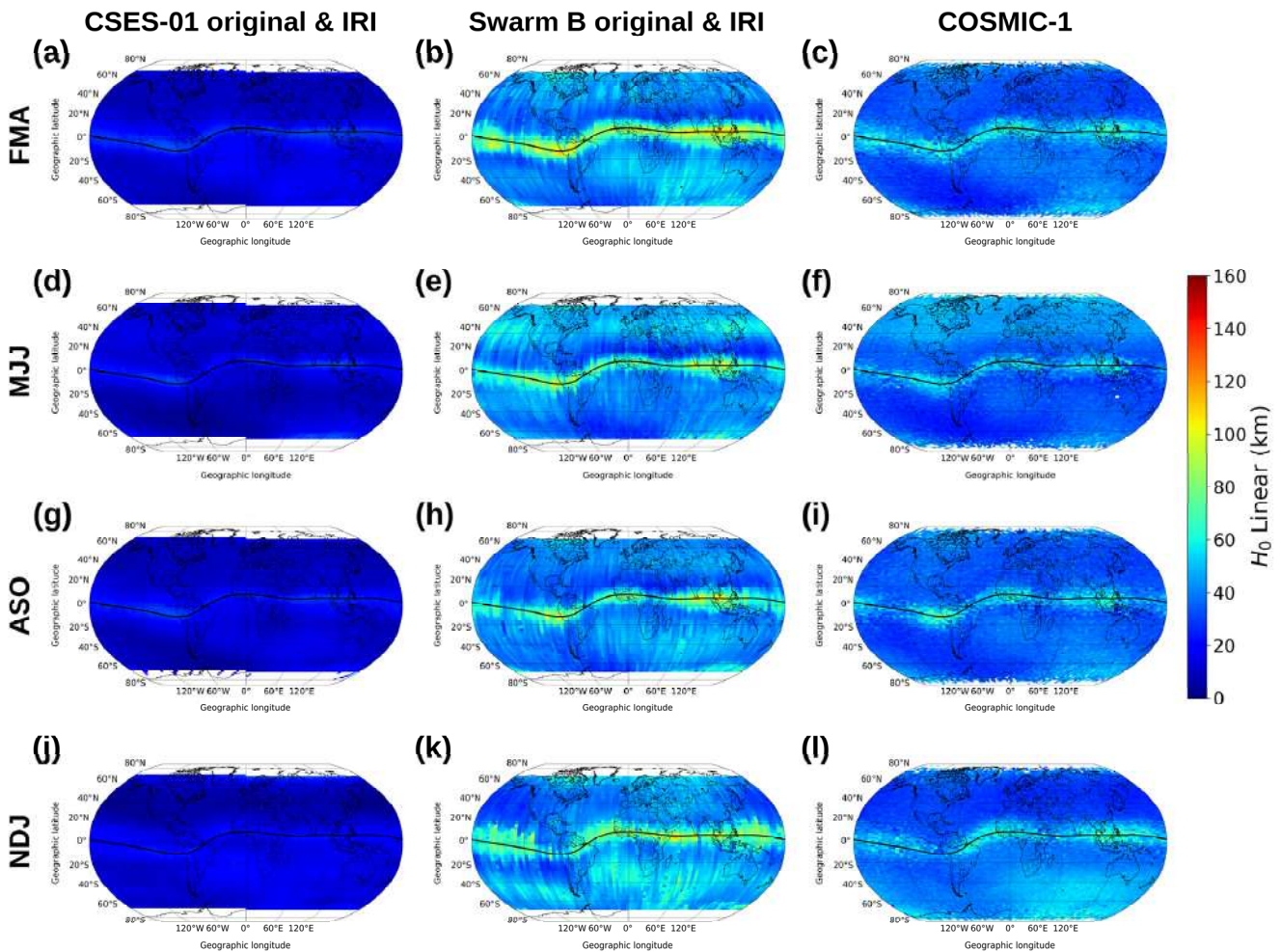## CSES-01, SWARM B, IRI → 2019—2021, COSMIC-1 → F10.7$_{81}$ ≤ 85 sfu

Figure 6. Geographical representation of median values of H_0 for the daytime sector (~14:00 LT). First row plots (panels (**a**–**c**)) refer to FMA = (February, March, April) months; second row plots (panels (**d**–**f**)) refer to MJJ = (May, June, July) months; third row plots (panels (**g**–**i**)) refer to ASO = (August, September, October) months; and fourth row plots (panels (**j**–**l**)) refer to NDJ = (November, December, January) months. First column plots (panels (**a**,**d**,**g**,**j**)) are H_0 values obtained with non-calibrated CSES—01 and IRI-modeled data; second column plots (panels (**b**,**e**,**h**,**k**)) are corresponding values obtained with non-calibrated Swarm B and IRI-modeled data; third column plots (panels (**c**,**f**,**i**,**l**)) are those obtained with COSMIC—1-measured N_e data by radio occultation. Color bar scale is the same across all panels. The solid black curve in each plot represents the geomagnetic equator.

The results in Figures 6 and 7 demonstrate the importance of calibrating both CSES—01 and Swarm B N_e values measured by LPs.

4.3. Topside Effective Scale Height Modeled through the Original NeQuick Formulation

It is worth highlighting that the linear approximation of the topside effective scale height produces scale height values different than those modeled through the original NeQuick formulation of Equation (5). To characterize the differences in both magnitude and spatial variation between the two modeling approaches, we re-calculated H_0 values by using directly the NeQuick topside effective scale height of Equation (5). In this way, dH/dz (which, in NeQuick, is represented by the parameter g) is kept constant and equal to 0.125, and any of its spatial variations are avoided. Figure 8 presents H_0 values obtained with the

NeQuick scale height formulation of Equation (5) applied to the CSES—01 N_e calibrated dataset. By comparing Figure 8 with Figures 4 and 5, it is clear how they show similar spatial patterns, albeit with different magnitudes. Specifically, the very high H_0 values during nighttime, at specific longitudinal sectors and which maximize during NDJ months, are still present. This comparison confirms the consistency of both topside modeling approaches in the range of altitudes sounded by CSES—01 and Swarm B satellites.
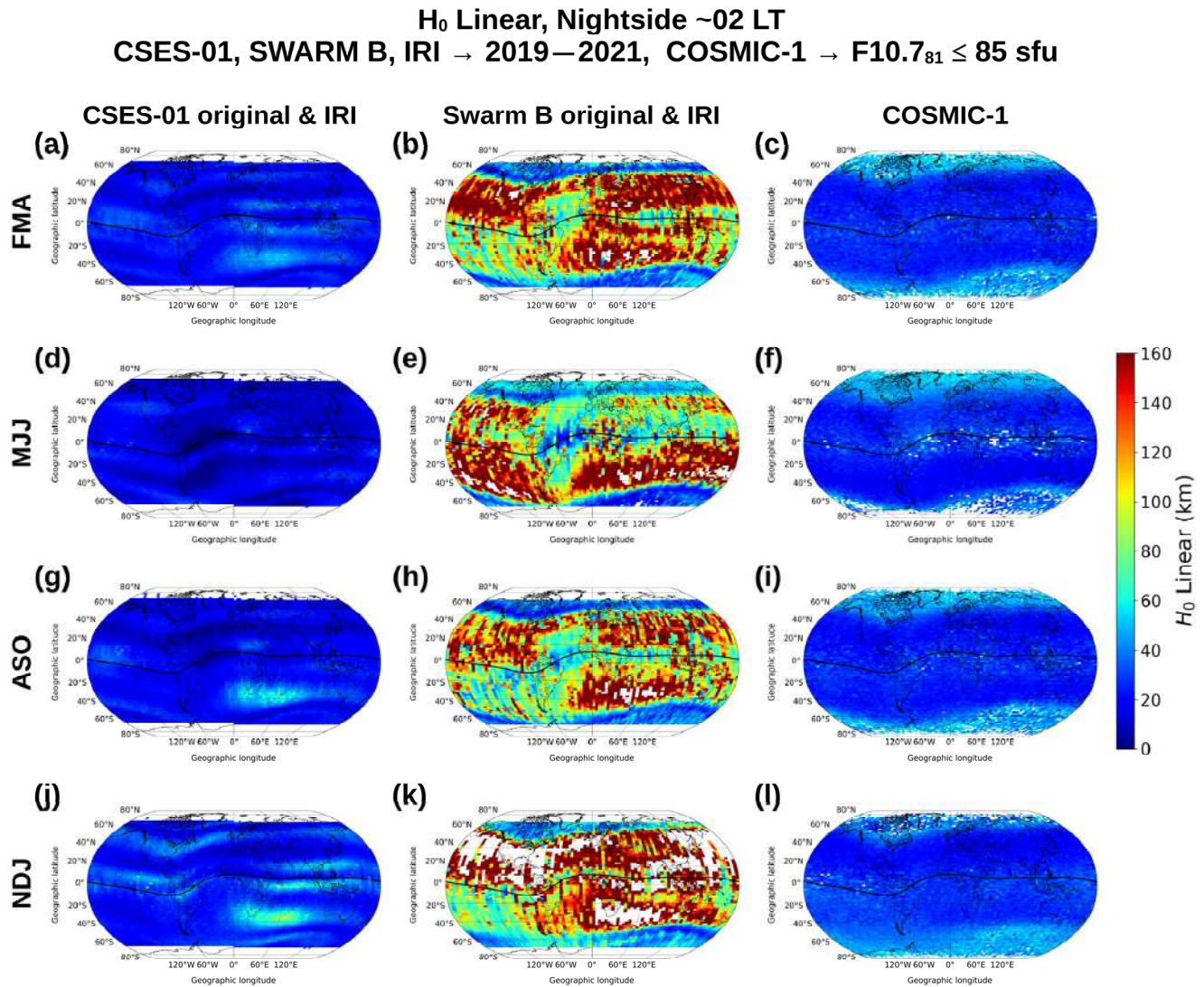

Figure 7. Geographical representation of median values of H_0 for the nighttime sector (~02:00 LT). First row plots (panels (**a**–**c**)) refer to FMA = (February, March, April) months; second row plots (panels (**d**–**f**)) refer to MJJ = (May, June, July) months; third row plots (panels (**g**–**i**)) refer to ASO = (August, September, October) months; and fourth row plots (panels (**j**–**l**)) refer to NDJ = (November, December, January) months. First column plots (panels (**a**,**d**,**g**,**j**)) are H_0 values obtained with non-calibrated CSES—01 and IRI-modeled data; second column plots (panels (**b**,**e**,**h**,**k**)) are corresponding values obtained with non-calibrated Swarm B and IRI-modeled data; third column plots (panels (**c**,**f**,**i**,**l**)) are those obtained with COSMIC—1-measured N_e data by radio occultation. Color bar scale is the same across all panels. The solid black curve in each plot represents the geomagnetic equator.
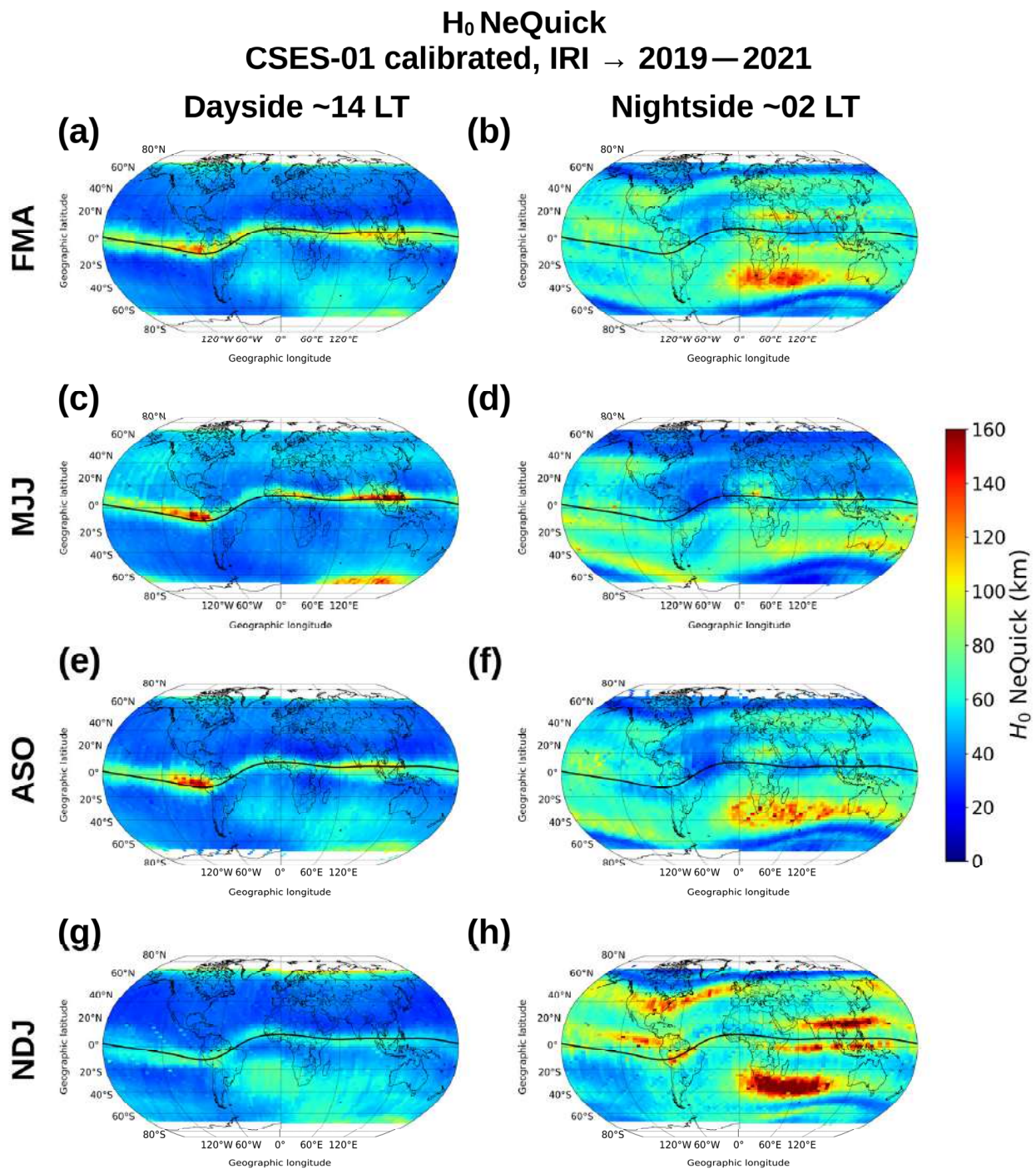
Figure 8. Geographical representation of median values of H_0 obtained with the original NeQuick topside effective scale height formulation applied to CSES—01 calibrated and IRI-modeled data. First row plots (panels (**a**,**b**)) refer to FMA = (February, March, April) months; second row plots (panels (**c**,**d**)) refer to MJJ = (May, June, July) months; third row plots (panels (**e**,**f**)) refer to ASO = (August, September, October) months; and fourth row plots (panels (**g**,**h**)) refer to NDJ = (November, December, January) months. First column plots (panels (**a**,**c**,**e**,**g**)) are for the daytime sector; second column plots (panels (**b**,**d**,**f**,**h**)) are for the nighttime sector. Color bar scale is the same across all panels. The solid black curve in each plot represents the geomagnetic equator.

4.4. Comparison between F2-Layer Peak Parameters Modeled by IRI and Measured by COSMIC—1

The accurate specification of the F2-layer peak anchor point has a significant role in topside profile modeling. Since, in our study, this task is assigned to the IRI model, we compared IRI-modeled F2-layer peak parameters with corresponding ones measured by COSMIC—1. We limit the comparison to the nighttime sector when the major discrepancies between modeled H_0 values have been found (see Figure 5). Figure 9 reports the IRI-modeled *hm*F2 values and those measured by COSMIC-1 for the nighttime sector. Figure 10 shows the corresponding plots for *Nm*F2. Figure 9 highlights the good agreement between modeled and measured *hm*F2 values, in terms of both magnitude and spatial variations, as noted by other studies [44,54–56]. This is somewhat expected because the Shubin *hm*F2 model [43] is based on COSMIC—1 RO data. Overall, IRI-modeled *hm*F2 values vary in a narrower range of magnitude compared to those of COSMIC—1, but they do not show any specific longitudinal variation that could account for the very high H_0 values modeled during nighttime.

Instead, the comparison between modeled and measured *Nm*F2 values (Figure 10), albeit showing a general agreement in magnitude, shows differences at specific longitudinal sectors. Focusing on NDJ months (panels g and h in Figure 10), where H_0 values calculated through CSES—01 and Swarm B observations maximize, IRI-modeled *Nm*F2 values have deep minima in the South Indian Ocean and in two bands at low latitudes in the Asian sector. COSMIC—1 also measures minima in those regions but to a lesser extent than IRI. Moreover, at low latitudes in the Asian sector, COSMIC—1 data do not show the two-band structure modeled by IRI. IRI-modeled nighttime *Nm*F2 values often show spatial variations that follow the geomagnetic field lines configuration. This is particularly evident in the already mentioned two minima bands in NDJ months in the Asian sector and also with respect to the relative maximum above the geomagnetic equator in the equinoctial months (panels a and e in Figure 10).
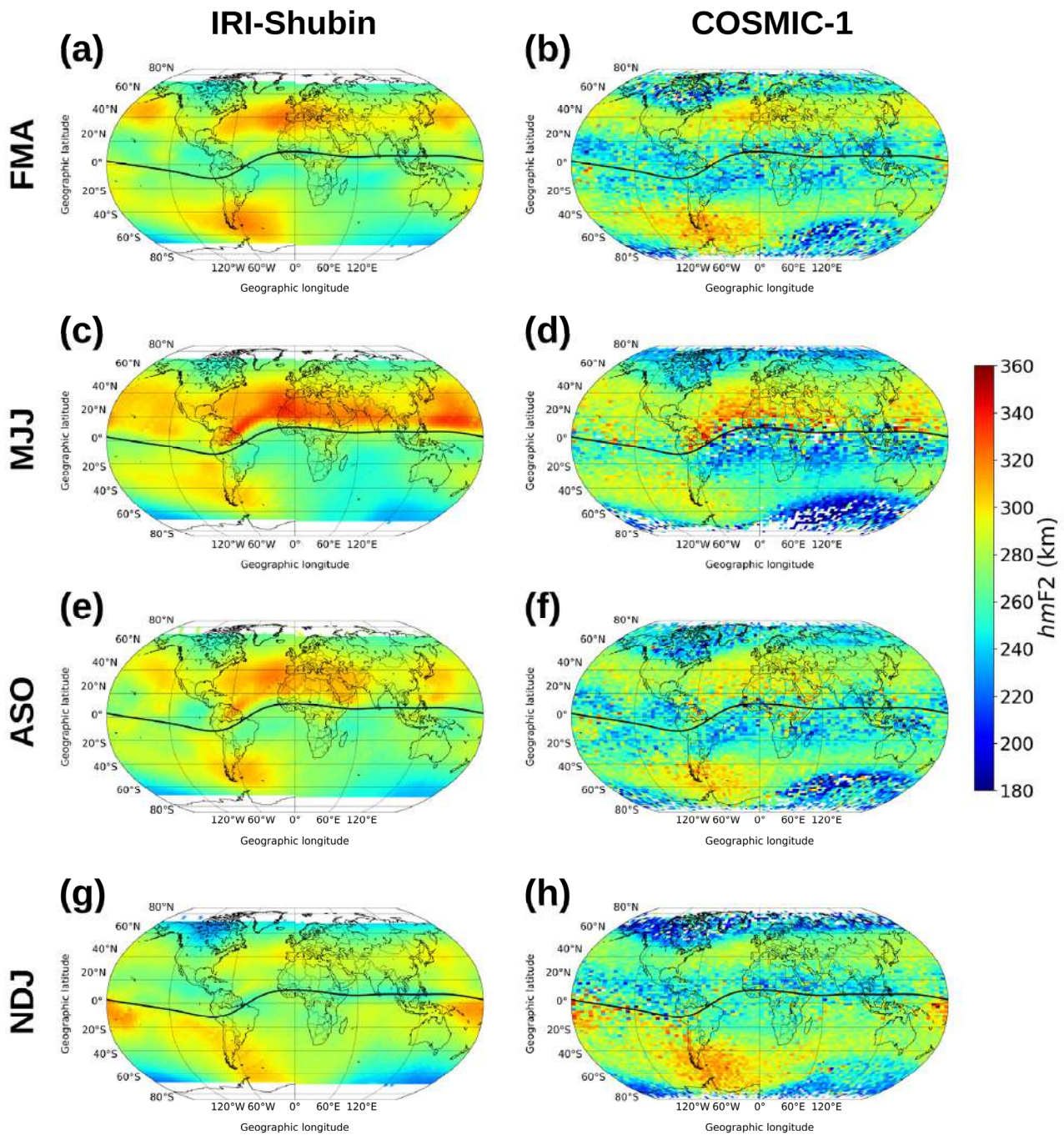
Figure 9. Geographical representation of median values of *hm*F2 for the nighttime sector (~02:00 LT). First row plots (panels (**a**,**b**)) refer to FMA = (February, March, April) months; second row plots (panels (**c**,**d**)) refer to MJJ = (May, June, July) months; third row plots (panels (**e**,**f**)) refer to ASO = (August, September, October) months; and fourth row plots (panels (**g**,**h**)) refer to NDJ = (November, December, January) months. First column plots (panels (**a**,**c**,**e**,**g**)) are *hm*F2 values, as modeled by IRI with the Shubin option; second column plots (panels (**b**,**d**,**f**,**h**)) are corresponding values, as obtained with COSMIC—1 radio occultation-measured values. Color bar scale is the same across all panels. The solid black curve in each plot represents the geomagnetic equator.
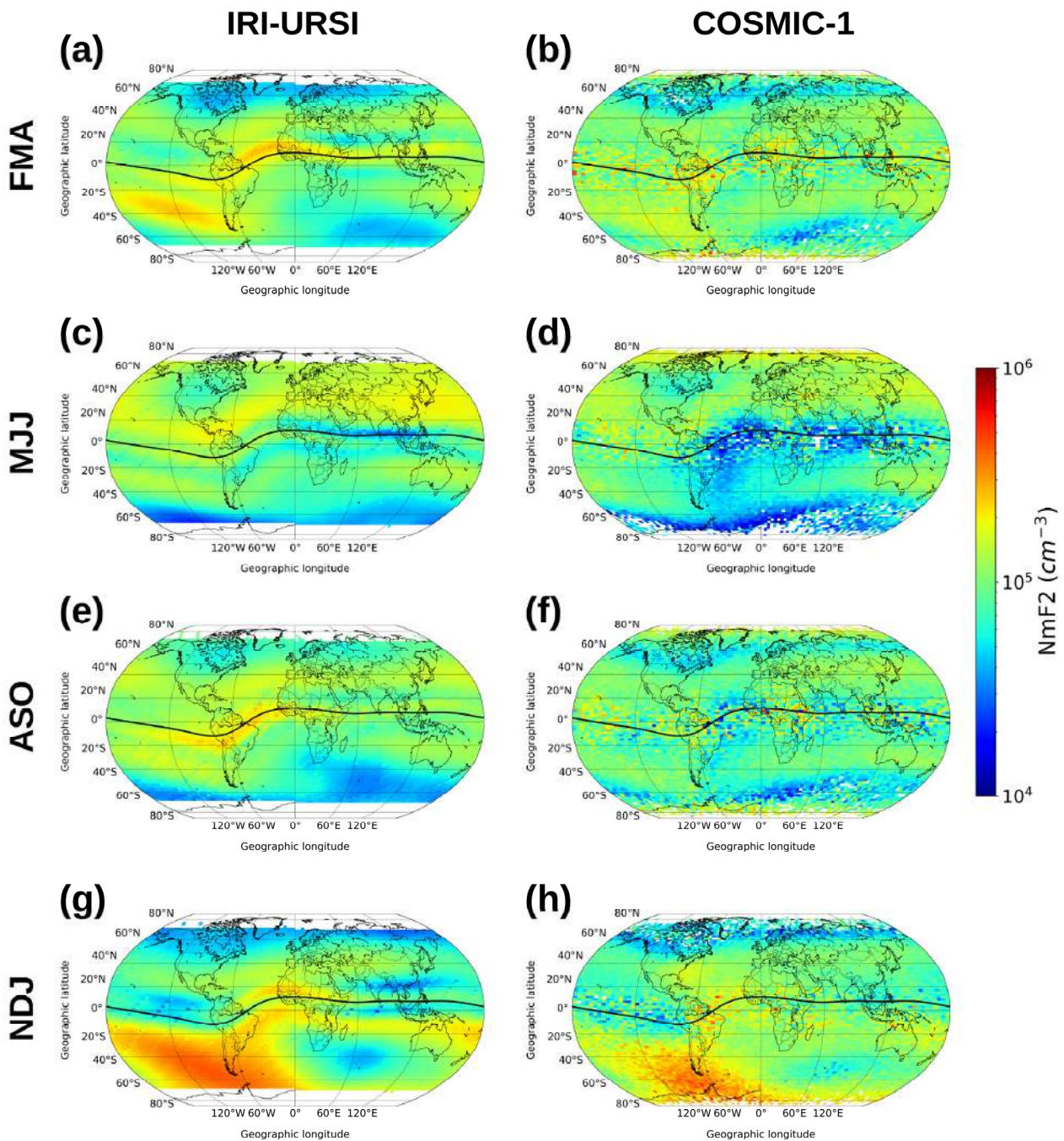
Figure 10. Geographical representation of median values of *Nm*F2 values for the nighttime sector (~02:00 LT). First row plots (panels (**a**,**b**)) refer to FMA = (February, March, April) months; second row plots (panels (**c**,**d**)) refer to MJJ = (May, June, July) months; third row plots (panels (**e**,**f**)) refer to ASO = (August, September, October) months; and fourth row plots (panels (**g**,**h**)) refer to r NDJ = (November, December, January) months. First column plots (panels (**a**,**c**,**e**,**g**)) are *Nm*F2 values, as modeled by IRI with URSI coefficients; second column plots (panels (**b**,**d**,**f**,**h**)) are corresponding values, as obtained with COSMIC—1 radio occultation-measured values. Color bar scale is the same across all panels. The solid black curve in each plot represents the geomagnetic equator.

5. Discussion

The results reported in Section 4 revealed that, during nighttime, there are remarkable differences between H_0 values obtained through calibrated CSES—01 and Swarm B N_e observations and those obtained through COSMIC—1 RO profiles (see Figure 5). On the contrary, during daytime, there is good agreement with differences in magnitude localized around the geomagnetic equator (see Figure 4). We rule out the presence of bias in the N_e topside anchor point because H_0 values obtained with both CSES—01 and Swarm B N_e-calibrated observations show the same spatial patterns. In fact, both LPs on CSES—01 and Swarm B should be affected by the same bias. Furthermore, the calibration procedure developed in [34] does not include any spatial variation, meaning that it cannot be the cause of the problem. This is verified by the results obtained with non-calibrated N_e values (Figures 6 and 7), which show similar spatial patterns but with a different magnitude.

A possible source of error could lie in the assumption made to apply the scale height linear approximation, i.e., in the modeled dH/dz values, which show large latitudinal variations during nighttime. To rule out this possibility, we re-calculated H_0 values by directly using the NeQuick topside effective scale height of Equation (5) in the NeQuick topside representation of Equation (4). The corresponding results have been shown in Figure 8 and compared with Figures 4 and 5. Since Figure 8 was obtained with a constant value of dH/dz, this excludes the possibility that the use of dH/dz values modeled through COSMIC—1 RO could bias the analysis during nighttime. This, in turn, attests to the reliability of the linear scale height assumption made in this work.

After excluding potential sources of error associated with the N_e topside anchor point and the linear scale height assumption, we looked into the possibility that the analysis may have been impacted by an incorrect representation of the F2-layer peak by the IRI model. To assess the accuracy of the F2-layer peak modeling by IRI, we compared IRI-modeled $NmF2$ and $hmF2$ values against those recorded by COSMIC—1 for the same conditions studied in this work. We focused on the nighttime sector, where there are the greatest discrepancies between H_0 values calculated through CSES—01 and Swarm B observations and COSMIC—1 RO profiles. Since the topside profile is anchored to the F2-layer peak point, an error in the modeling of $NmF2$ can have a deep impact on modeled scale height values. With a fixed topside anchor point, an increase in $NmF2$ would reduce H because, to join the topside anchor point, the electron density has to decrease at a faster vertical rate. On the contrary, a decrease in $NmF2$ would increase H because the electron density has to drop at a slower vertical rate in order to join the topside anchor point. In light of these considerations, an $NmF2$ underestimation by IRI has the effect of overestimating the topside scale height and then H_0. This explains the H_0 high values during nighttime in the South Indian Ocean and in two bands at low latitudes in the Asian sector (see Figure 5), which are associated with underestimated $NmF2$ values by IRI (see Figure 10).

The spatial variations in IRI nighttime $NmF2$ values could be attributed to the spherical harmonics analysis underlying the $NmF2$ modeling. In fact, the IRI $NmF2$ model is based on the spherical harmonics numerical mapping procedure pioneered by the authors of [57–59] and later extended by the authors of [42]. According to this mapping, the latitudinal dependence is described by the modified dip latitude (modip, [10]), which was introduced by the author of [60] to better describe the ionospheric variations in equatorial and polar regions. Modip is equal to the magnetic dip inclination at low latitudes, while it is closer to the geographic latitude at higher latitudes. Some of the spatial variations exhibited by the IRI-modeled $NmF2$ nighttime values, and in turn by the modeled H_0 values, strictly follow modip isolines (see Figure 14 in [10]), which are a signature of spherical harmonics. This behavior highlights a mismodeling in the $NmF2$ spatial variations, which is limited to the nighttime sector. In fact, the same issue does not affect the daytime sector.

This agrees with the IRI F2-layer peak characteristics validation analysis performed by the authors of [44]. A comparison with values measured by 40 ground-based ionosondes and by COSMIC—1 RO highlighted a local time dependence in the IRI $NmF2$ performance [44]. The comparison involving ionosonde-measured values showed that IRI has a

Normalized Root Mean Square Error (NRMSE) value of 14.861% during daytime and of 23.790% during nighttime (see Table 2 in [44]). The comparison involving NmF2 values from COSMIC—1 RO measurements showed that IRI has a NRMSE value of 14.841% during daytime and 21.781% during nighttime (see Table 4 in [44]). A possible cause of the worse performance by IRI during nighttime could be attributed to the sub-optimal spatial representation highlighted in the left column plots of Figure 10. This is the most likely cause of the H_0 misrepresentation obtained during nighttime.

6. Conclusions

In situ N_e observations by LPs onboard CSES—01 and Swarm B satellites have been used to characterize the global behavior of the effective scale height (H_0) at the F2-layer peak. For the F2-layer peak anchor point, we used values modeled by the latest version of IRI, i.e., IRI—2020. The dataset used in this study allowed for the investigation of the H_0 global behavior for both daytime and nighttime conditions, different seasons, and low solar activity.

The main results of this work can be summarized as follows:

1. For daytime conditions, H_0 values modeled using CSES—01 and Swarm B calibrated observations agree with corresponding values obtained directly from COSMIC—1 RO profiles, which is our reference. The geomagnetic equator is where the most relevant differences are present. There, values modeled through both CSES—01 and Swarm B observations are much higher than those obtained through COSMIC—1. Instead, during nighttime, H_0 values obtained from both CSES—01 and Swarm B-calibrated observations show large differences compared to those obtained through COSMIC—1. Such differences are spatially localized in several latitudinal belts at both low and mid latitudes, where H_0 values obtained from both CSES—01 and Swarm B show values much higher in magnitude than those from COSMIC—1.

2. H_0 values obtained with non-calibrated CSES—01 and Swarm B observations differ substantially from those obtained with calibrated observations. Except for the Swarm B daytime sector, H_0 values from non-calibrated observations show either highly underestimated or overestimated values, which, in most cases, are unphysical. This is an independent piece of evidence that suggest that, for the local times and low solar activity conditions studied in this paper, both CSES—01 and Swarm B LP N_e observations need to be calibrated before being used for ionospheric modeling.

3. Most of the H_0 mismodeling for nighttime conditions seems to be caused by a sub-optimal spatial representation of the F2-layer peak density made by the IRI model. This issue could be attributed to the IRI spherical harmonics numerical mapping procedure underlying the NmF2 spatial representation, which shows some limitation during nighttime hours. However, the issue is not present for daytime hours. This highlights the importance of an accurate characterization of the F2-layer peak anchor point in topside ionosphere modeling.

The methodology developed in this study for the topside effective scale height modeling turns out to be applicable to any in situ N_e observation made by LEO satellites orbiting in the topside ionosphere. At the same time, the reliability of the method is critically dependent on the accurate knowledge of both the topside anchor point and the F2-layer peak anchor point. This is an undoubted disadvantage when compared to the methodologies which make use of the full topside N_e profile provided by RO observations [6,25,51,61]. However, when accurate data are available, both spatial and time variations of the topside effective scale height can be reliably described.

In this study, the topside effective scale height variations due to the solar activity and geomagnetic disturbed conditions have not been investigated due to the limited dataset encompassing only low solar activity and fairly geomagnetically quiet conditions. As a future development, we plan to extend this study by also considering different solar activity and geomagnetic activity conditions when enough satellite observations will be available during the upcoming solar activity maximum.

The ever-increasing number of LEO satellites performing in situ N_e observations in the topside ionosphere makes the applicability of this methodology promising for topside ionosphere modeling. Ionospheric empirical models, such as IRI [10] and NeQuick [11], would benefit from an improved description of H_0, which in turn would improve the modeling of the topside profile shape. Moreover, since the scale height at the F2-layer peak (H_0) is tightly connected to the ionospheric equivalent slab thickness [62–65], a better characterization of H_0 would also help in understanding the physical processes driving the plasma distribution in the ionosphere.

Author Contributions: Conceptualization, A.P. and M.P. (Michael Pezzopane); methodology, A.P., M.P. (Michael Pezzopane) and B.N.; software, A.P.; data curation, A.P., I.C. and M.P. (Mirko Piersanti); investigation, A.P., M.P. (Michael Pezzopane), and B.N.; validation, A.P.; formal analysis, A.P.; writing—original draft preparation, A.P.; writing—review and editing, all authors; funding acquisition, P.D.M. All authors have read and agreed to the published version of the manuscript.

Data Availability Statement: CSES—01 data are publicly available at https://www.leos.ac.cn/ (accessed on the 7 April 2023) after registration. ESA Swarm data are publicly available at https://earth.esa.int/eogateway/missions/swarm/data (accessed on 7 April 2023). COSMIC—1 RO data are stored in the COSMIC Data Analysis and Archive Center (CDAAC, http://cdaac-www.cosmic.ucar.edu/cdaac/products.html, accessed on the 7 April 2023). F10.7 solar index data were downloaded through the OMNIWeb Data Explorer website (https://omniweb.gsfc.nasa.gov/form/dx1.html, accessed on 7 April 2023) maintained by the NASA. IRI Fortran code is available on the IRI website (http://irimodel.org/, accessed on the 7 April 2023).

Conflicts of Interest: The authors declare no conflict of interest.

References

1. Rishbeth, H.; Garriott, O. *Introduction to Ionospheric Physics*; International Geophysics Series; Academic Press: New York, NY, USA, 1969; Volume 14.
2. Hargreaves, J.K. *The Solar-Terrestrial Environment*; Cambridge University Press: New York, NY, USA, 1992.
3. Ratcliffe, J.A. *An Introduction to the Ionosphere and Magnetosphere*; Cambridge University Press: Cambridge, UK, 1972.
4. Liu, L.; Le, H.; Wan, W.; Sulzer, M.P.; Lei, J.; Zhang, M.-L. An analysis of the scale heights in the lower topside ionosphere based on the Arecibo incoherent scatter radar measurements. *J. Geophys. Res.* **2007**, *112*, A06307. [CrossRef]
5. Liu, L.; Wan, W.; Zhang, M.-L.; Ning, B.; Zhang, S.-R.; Holt, J.M. Variations of topside ionospheric scale height over Millstone Hill during the 30-day incoherent scatter radar experiment. *Ann. Geophys.* **2007**, *25*, 2019–2027. [CrossRef]
6. Pignalberi, A.; Pezzopane, M.; Nava, B.; Coïsson, P. On the link between the topside ionospheric effective scale height and the plasma ambipolar diffusion, theory and preliminary results. *Sci. Rep.* **2020**, *10*, 17541. [CrossRef] [PubMed]
7. Pignalberi, A.; Pezzopane, M.; Rizzi, R. Modelling the lower part of the topside ionospheric vertical electron density profile over the European region by means of Swarm satellites data and IRI UP method. *Space Weather* **2018**, *16*, 304–320. [CrossRef]
8. Stankov, S.M.; Jakowski, N.; Heise, S.; Muhtarov, P.; Kutiev, I.; and Warnant, R. A new method for reconstruction of the vertical electron density distribution in the upper ionosphere and plasmasphere. *J. Geophys. Res.* **2003**, *108*, 1164. [CrossRef]
9. Verhulst, T.; Stankov, S.M. Evaluation of ionospheric profilers using topside sounding data. *Radio Sci.* **2014**, *49*, 181–195. [CrossRef]
10. Bilitza, D.; Pezzopane, M.; Truhlik, V.; Altadill, D.; Reinisch, B.W.; Pignalberi, A. The International Reference Ionosphere model: A review and description of an ionospheric benchmark. *Rev. Geophys.* **2022**, *60*, e2022RG000792. [CrossRef]

11. Nava, B.; Coïsson, P.; Radicella, S. A new version of the NeQuick ionosphere electron density model. *J. Atmos. Sol.-Terr. Phys.* **2008**, *70*, 1856–1862. [CrossRef]

12. Themens, D.R.; Jayachandran, P.T.; Galkin, I.; Hall, C. The Empirical Canadian High Arctic Ionospheric Model (E-CHAIM): NmF2 and hmF2. *J. Geophys. Res. Space Phys.* **2017**, *122*, 9015–9031. [CrossRef]

13. Hunsucker, R.D. *Radio Techniques for Probing the Terrestrial Ionosphere*; Springer: Berlin/Heidelberg, Germany, 1991. [CrossRef]

14. Pignalberi, A.; Pezzopane, M.; Tozzi, R.; De Michelis, P.; Coco, I. Comparison between IRI and preliminary Swarm Langmuir probe measurements during the St. Patrick storm period. *Earth Planets Space* **2016**, *68*, 93. [CrossRef]

15. Shen, X.H.; Zhang, X.M.; Yuan, S.G.; Wang, L.W.; Cao, J.B.; Huang, J.P.; Zhu, X.H.; Picozza, P.; Dai, J.P. The state-of-the-art of the China Seismo-Electromagnetic Satellite mission. *Sci. China Technol. Sci.* **2018**, *61*, 634–642. [CrossRef]

16. Friis-Christensen, E.; Lühr, H.; Knudsen, D.; Haagmans, R. Swarm—An earth observation mission investigating geospace. *Adv. Space Res.* **2008**, *41*, 210–216. [CrossRef]

17. Pignalberi, A.; Pezzopane, M.; Rizzi, R.; Galkin, I. Effective solar indices for ionospheric modelling: A review and a proposal for a real-time regional IRI. *Surv. Geophys.* **2018**, *39*, 125–167. [CrossRef]

18. Pezzopane, M.; Pignalberi, A. The ESA Swarm mission to help ionospheric modelling: A new NeQuick topside formulation for mid-latitude regions. *Sci. Rep.* **2019**, *9*, 12253. [CrossRef]

19. Coïsson, P.; Radicella, S.M.; Leitinger, R.; Nava, B. Topside electron density in IRI and NeQuick: Features and limitations. *Adv. Space Res.* **2006**, *37*, 937–942. [CrossRef]

20. Nava, B.; Radicella, S.M.; Pulinets, S.; Depuev, V. Modelling bottom and topside electron density and TEC with profile data from topside ionograms. *Adv. Space Res.* **2001**, *27*, 31–34. [CrossRef]

21. Olivares-Pulido, G.; Hernández-Pajares, M.; Aragón-Àngel, A.; Garcia-Rigo, A. A linear scale height chapman model supported by GNSS occultation measurements. *J. Geophys. Res. Space Phys.* **2016**, *121*, 7932–7940. [CrossRef]

22. Hernández-Pajares, M.; Garcia-Fernàndez, M.; Rius, A.; Notarpietro, R.; von Engeln, A.; Olivares-Pulido, G.; Aragón-Àngel, À.; García-Rigo, A. Electron density extrapolation above F2 peak by the linear Vary-Chap model supporting new Global Navigation Satellite Systems-LEO occultation missions. *J. Geophys. Res. Space Phys.* **2017**, *122*, 9003–9014. [CrossRef]

23. dos Santos Prol, F.; Themens, D.R.; Hernández-Pajares, M.; de Oliveira Camargo, P.; de Assis Honorato Muella, M.T. Linear vary-chap topside electron density model with topside sounder and radio-occultation data. *Surv. Geophys.* **2019**, *40*, 277–293. [CrossRef]

24. Prol, F.S.; Smirnov, A.G.; Hoque, M.M.; Shprits, Y.Y. Combined model of topside ionosphere and plasmasphere derived from radio-occultation and Van Allen Probes data. *Sci. Rep.* **2022**, *12*, 9732. [CrossRef]

25. Pignalberi, A.; Pezzopane, M.; Themens, D.R.; Haralambous, H.; Nava, B.; Coïsson, P. On the Analytical Description of the Topside Ionosphere by NeQuick: Modelling the Scale Height through COSMIC/FORMOSAT-3 Selected Data. *IEEE J. Sel. Top. Appl. Earth Obs. Remote Sens.* **2020**, *13*, 1867–1878. [CrossRef]

26. Smirnov, A.; Shprits, Y.; Prol, F.; Lühr, H.; Berrendorf, M.; Zhelavskaya, I.; Xiong, C. A novel neural network model of Earth's topside ionosphere. *Sci. Rep.* **2023**, *13*, 1303. [CrossRef] [PubMed]

27. Anthes, R.; Bernhardt, P.A.; Chen, Y.; Cucurull, L.; Dymond, K.F.; Ector, D.; Healy, S.B.; Ho, S.-P.; Hunt, D.C.; Kuo, Y.-H.; et al. The COSMIC/FORMOSAT-3 mission: Early results. *Bull. Amer. Meteorol. Soc.* **2008**, *89*, 313–333. [CrossRef]

28. Yan, R.; Guan, Y.; Shen, X.; Huang, J.; Zhang, X.; Liu, C.; Liu, D. The Langmuir Probe onboard CSES: Data inversion analysis method and first results. *Earth Plan. Phys.* **2018**, *2*, 479–488. [CrossRef]

29. Liu, C.; Guan, Y.; Zheng, X.; Zhang, A.; Piero, D.; Sun, Y. The technology of space plasma in-situ measurement on the China Seismo-Electromagnetic Satellite. *Sci. China Technol. Sci.* **2019**, *62*, 829–838. [CrossRef]

30. Wang, X.; Cheng, W.; Yang, D.; Liu, D. Preliminary validation of in situ electron density measurements onboard CSES using observations from Swarm Satellites. *Adv. Space Res.* **2019**, *64*, 982–994. [CrossRef]

31. Yan, R.; Zhima, Z.; Xiong, C.; Shen, X.; Huang, J.; Guan, Y.; Zhu, X.; Liu, C. Comparison of electron density and temperature from the CSES satellite with other space-borne and ground-based observations. *J. Geophys. Res. Space Phys.* **2020**, *125*, e2019JA027747. [CrossRef]

32. Liu, J.; Guan, Y.; Zhang, X.; Shen, X. The data comparison of electron density between CSES and DEMETER satellite, Swarm constellation and IRI model. *Earth Space Sci.* **2021**, *8*, e2020EA001475. [CrossRef]

33. Liu, J.; Xu, T.; Ding, Z.; Zhang, X. The Comparison of Electron Density between CSES In Situ and Ground-Based Observations in China. *Remote Sens.* **2022**, *14*, 4498. [CrossRef]

34. Pignalberi, A.; Pezzopane, M.; Coco, I.; Piersanti, M.; Giannattasio, F.; De Michelis, P.; Tozzi, R.; Consolini, G. Inter-Calibration and Statistical Validation of Topside Ionosphere Electron Density Observations Made by CSES—01 Mission. *Remote Sens.* **2022**, *14*, 4679. [CrossRef]

35. Knudsen, D.J.; Burchill, J.K.; Buchert, S.C.; Eriksson, A.I.; Gill, R.; Wahlund, J.-E.; Åhlen, L.; Smith, M.; Moffat, B. Thermal ion imagers and Langmuir probes in the Swarm electric field instruments. *J. Geophys. Res. Space Phys.* **2017**, *122*, 2655–2673. [CrossRef]

36. Lomidze, L.; Knudsen, D.J.; Burchill, J.; Kouznetsov, A.; Buchert, S.C. Calibration and validation of Swarm plasma densities and electron temperatures using ground-based radars and satellite radio occultation measurements. *Radio Sci.* **2018**, *53*, 15–36. [CrossRef]

37. Catapano, F.; Buchert, S.; Qamili, E.; Nilsson, T.; Bouffard, J.; Siemes, C.; Coco, I.; D'Amicis, R.; Tøffner-Clausen, L.; Trenchi, L.; et al. Swarm Langmuir probes' data quality validation and future improvements. *Geosci. Instrum. Method. Data Syst.* **2022**, *11*, 149–162. [CrossRef]

38. Pakhotin, I.P.; Burchill, J.K.; Förster, M.; Lomidze, L. The swarm Langmuir probe ion drift, density and effective mass (SLIDEM) product. *Earth Planets Space* **2022**, *74*, 109. [CrossRef]

39. Smirnov, A.; Shprits, Y.; Zhelavskaya, I.; Lühr, H.; Xiong, C.; Goss, A.; Prol, F.S.; Schmidt, M.; Hoque, M.; Pedatella, N.; et al. Intercalibration of the plasma density measurements in Earth's topside ionosphere. *J. Geophys. Res. Space Phys.* **2021**, *126*, e2021JA029334. [CrossRef]

40. Xiong, C.; Jiang, H.; Yan, R.; Lühr, H.; Stolle, C.; Yin, F.; Smirnov, A.; Piersanti, M.; Liu, Y.; Wan, X.; et al. Solar flux influence on the in-situ plasma density at topside ionosphere measured by Swarm satellites. *J. Geophys. Res. Space Phys.* **2022**, *127*, e2022JA030275. [CrossRef]

41. Bilitza, D. IRI the International Standard for the Ionosphere. *Adv. Radio Sci.* **2018**, *16*, 1–11. [CrossRef]

42. Rush, C.M.; Fox, M.; Bilitza, D.; Davies, K.; McNamara, L.; Stewart, F.G.; PoKempner, M. Ionospheric mapping-an update of foF2 coefficients. *Telecommun. J.* **1989**, *56*, 179–182.

43. Shubin, V.N. Global median model of the F2-layer peak height based on ionospheric radio-occultation and ground based digisonde observations. *Adv. Space Res.* **2015**, *56*, 916–928. [CrossRef]

44. Pignalberi, A.; Pietrella, M.; Pezzopane, M. Towards a Real-Time Description of the Ionosphere: A Comparison between International Reference Ionosphere (IRI) and IRI Real-Time Assimilative Mapping (IRTAM) Models. *Atmosphere* **2021**, *12*, 1003. [CrossRef]

45. Haji, G.A.; Romans, L.J. Ionospheric electron density profiles obtained with the global positioning system: Results from the GPS/MET experiment. *Radio Sci.* **1998**, *33*, 175–190. [CrossRef]

46. Schreiner, W.S.; Sokolovskiy, S.V.; Rocken, C.; Hunt, D.C. Analysis and validation of GPS/MET radio occultation data in the ionosphere. *Radio Sci.* **1999**, *34*, 949–966. [CrossRef]

47. Garcia-Fernandez, M.; Hernandez-Pajares, M.; Juan, J.M.; Sanz, J. Improvement of ionospheric electron density estimation with GPSMET occultations using Abel inversion and VTEC information. *J. Geophys. Res. Space Phys.* **2003**, *108*, 1338. [CrossRef]

48. Yue, X.; Schreiner, W.S.; Lei, J.; Sokolovskiy, S.V.; Rocken, C.; Hunt, D.C.; Kuo, Y.H. Error analysis of Abel retrieved electron density profiles from radio occultation measurements. *Ann. Geophys.* **2010**, *28*, 217–222. [CrossRef]

49. *UCAR COSMIC Program, 2022*; COSMIC—1 Data Products ionPrf. UCAR/NCAR—COSMIC: Boulder, CO, USA, 2022. [CrossRef]

50. Tapping, K.F. The 10.7 cm solar radio flux (F10.7). *Space Weather* **2013**, *11*, 394–406. [CrossRef]

51. Pignalberi, A.; Pezzopane, M.; Nava, B. Optimizing the NeQuick topside scale height parameters through COSMIC/FORMOSAT-3 radio occultation data. *IEEE Geosc. Rem. Sens. Lett.* **2022**, *19*, 8017005. [CrossRef]

52. Laundal, K.M.; Richmond, A.D. Magnetic Coordinate Systems. *Space Sci. Rev.* **2017**, *206*, 27. [CrossRef]

53. Themens, D.R.; Jayachandran, P.T.; Bilitza, D.; Erickson, P.J.; Häggström, I.; Lyashenko, M.V.; Reid, B.; Varney, R.H.; Pustovalova, L. Topside electron density representations for middle and high latitudes: A topside parameterization for E-CHAIM based on the NeQuick. *J. Geophys. Res. Space Phys.* **2018**, *123*, 1603–1617. [CrossRef]

54. Mengist, C.K.; Yadav, S.; Kotulak, K.; Bahar, A.; Zhang, S.-R.; Seo, K.-H. Validation of International Reference Ionosphere model (IRI-2016) for F-region peak electron density height (hmF2): Comparison with incoherent scatter radar (ISR) and ionosonde measurements at Millstone Hill. *Adv. Space Res.* **2020**, *65*, 2773–2781. [CrossRef]

55. Huang, H.; Moses, M.; Volk, A.E.; Elezz, O.A.; Kassamba, A.A.; Bilitza, D. Assessment of IRI-2016 hmF2 model options with digisonde, COSMIC observations for low and high solar flux conditions during 23rd solar cycle. *Adv. Space Res.* **2021**, *68*, 2093–2103. [CrossRef]

56. Moses, M.; Bilitza, D.; Kumar Panda, S.; Ochonugor, B.J. Assessment of IRI-2016 hmF2 model predictions with COSMIC observations over the African region. *Adv. Space Res.* **2021**, *68*, 2115–2123. [CrossRef]

57. Jones, W.B.; Gallet, R.M. Representation of diurnal and geographical variations of ionospheric data by numerical methods. *J. Res. Natl. Bur. Stand.* **1962**, *66*, 129–147. [CrossRef]

58. Jones, W.B.; Gallet, R.M. Representation of diurnal and geographic variations of ionospheric data by numerical methods, II. Control of instability. *ITU Telecommun. J.* **1965**, *32*, 18–28.

59. Jones, W.B.; Graham, R.P.; Leftin, M. Advances in ionospheric mapping by numerical methods. In *ESSA Technical Report ERL 107-ITS75*; U.S. Department of Commerce: Washington, DC, USA, 1969.

60. Rawer, K. Propagation of decameter waves (HF band). In *Meteorological and Astronomical Influences on Radio Wave Propagation*; Landmark, B., Ed.; Academic Press: Cambridge, MA, USA, 1963; pp. 221–250.

61. Li, Q.; Liu, L.; He, M.; Huang, H.; Zhong, J.; Yang, N.; Zhang, M.-L.; Jiang, J.; Chen, Y.; Le, H.; et al. A global empirical model of electron density profile in the F region ionosphere basing on COSMIC measurements. *Space Weather* **2021**, *19*, e2020SW002642. [CrossRef]

62. Pignalberi, A.; Nava, B.; Pietrella, M.; Cesaroni, C.; Pezzopane, M. Midlatitude climatology of the ionospheric equivalent slab thickness over two solar cycles. *J. Geod.* **2021**, *95*, 124. [CrossRef]

63. Pignalberi, A.; Pietrella, M.; Pezzopane, M.; Nava, B.; Cesaroni, C. The Ionospheric Equivalent Slab Thickness: A Review Supported by a Global Climatological Study over Two Solar Cycles. *Space Sci. Rev.* **2022**, *218*, 37. [CrossRef]

64. Titheridge, J.E. The slab thickness of the mid-latitude ionosphere. *Planet. Space Sci.* **1973**, *21*, 1775–1793. [CrossRef]
65. Jakowski, N.; Hoque, M.; Mielich, J.; Hall, C. Equivalent slab thickness of the ionosphere over Europe as an indicator of long-term temperature changes in the thermosphere. *J. Atmos. Sol.-Terr. Phys.* **2017**, *163*, 91–102. [CrossRef]